





Which filaments matter: the relative scalings of anisotropic infall

Junsup Shim^{1,2} ^{*}, Dmitri Pogosyan³ ^{**}, Myoungwon Jeon⁴ ^{***}, and Christophe Pichon^{4,5} ^{****}

¹ Department of Earth Sciences, Pusan National University, Busan 46241, Republic of Korea

² Academia Sinica Institute of Astronomy and Astrophysics (ASIAA), No. 1, Section 4, Roosevelt Road, Taipei 106216, Taiwan

³ Department of Physics, University of Alberta, 11322-89 Avenue, Edmonton, Alberta, T6G 2G7, Canada.

⁴ Department of Astronomy & Space Science, Kyung Hee University, 1732 Deogyong-daero, Yongin-si, Gyeonggi-do 17104, Republic of Korea

⁵ Institut d'Astrophysique de Paris, 98 bis Boulevard Arago, F-75014 Paris, France

April 6, 2026

ABSTRACT

Dark-matter haloes do not form in isolation but within the surrounding cosmic web. By the time a halo begins to collapse, its larger-scale environment has typically collapsed along two axes, forming filaments that channel anisotropic infall toward the halo. In this work, we derive from first principles the characteristic Lagrangian scale ratio at which such an anisotropic tidal field most strongly influences halo formation. Specifically, we identify the inflection point of the conditional probability that the tidal field, smoothed on a scale R_{sd} , undergoes two-dimensional compression, given the presence of a density peak of rarity ν on a smaller scale R_{pk} . For a standard Λ CDM cosmology, we find $(R_{\text{sd}}/R_{\text{pk}})_{\text{infl}} \approx 2.2 + (\nu - 2.5)$ for R_{pk} corresponding to a tophat filter of $8\text{Mpc}/h$. This result implies that the anisotropic tidal influence on a collapsing halo typically extends to 2–3 times the size of its Lagrangian patch. Recast as a function of formation redshift z , the characteristic filament scale around 2.5σ peaks can be approximated by $R_{\text{sd}}(z) \approx 31/(2 + (1 + z)^2)h^{-1}\text{Mpc}$. We provide practical scaling laws for selecting dynamically relevant smoothing scales in large-scale surveys and for setting initial patch sizes in high-resolution zoom simulations.

Key words. cosmic web – cosmology: large-scale structure of Universe – dark matter – galaxies: haloes – methods: analytical – methods: statistical

1. Introduction

Large-scale cosmic filaments are massive, thread-like structures of galaxies and dark matter (de Lapparent et al. 1986; Klypin & Shandarin 1993) that emerge as manifestations of the anisotropies of the underlying tidal field (Zel'dovich 1970; Bond et al. 1996). By channeling the anisotropic infall of matter and gas, these filaments serve as the supply lines for halos and galaxies at all redshifts, influencing their assembly histories (Hahn et al. 2009; Borzyszkowski et al. 2017; Tojeiro et al. 2017; Musso et al. 2018). Consequently, different tidal environmental factors – including proximity to filaments (Musso et al. 2018), their spatial orientation (Codis et al. 2015), and local connectivity (Codis et al. 2018) – drive distinct variations in the physical and dynamical properties of halos and galaxies, ranging from mass and morphology to abundance, color, luminosity, spin, and star formation (Aragón-Calvo et al. 2007; Hahn et al. 2007; Sousbie et al. 2008; Codis et al. 2012; Libeskind et al. 2012; Laigle et al. 2015; Shim et al. 2015; Kraljic et al. 2018, 2019; Laigle et al. 2018; Shim & Lee 2018; Kraljic et al. 2020; Song et al. 2021; Lee et al. 2021; Jhee et al. 2022; Arora et al. 2025; Yu et al. 2025).

While tidal characteristics are recognized as key factors in shaping galaxy properties, the characteristic scale of the surrounding filamentary structure is often treated as a fixed parameter. Although multiscale filament-finding algorithms exist (e.g.,

DisPerSE (Sousbie 2011)), the qualitative and quantitative variations between filaments identified at different scales relative to a given halo have not been systematically explored. In particular, the typical relative scale on which filaments contribute to halo dynamics remains poorly constrained. This leads to a fundamental question: does the influence of a filament on halos depend on its relative scale, and if so, is there a characteristic scale at which the filamentary environment most strongly governs the dynamics of haloes of a given rarity?

We address this question from first principles using Gaussian Random Field (GRF) theory, which effectively captures the statistics of cosmic fields, e.g., the underlying density and tidal fields, while relying on excursion set theory (Bond et al. 1991). By computing the joint probability distribution functions (JPDFs) of GRF variables under specific topological constraints – such as density peaks characterized by negative curvature – this formalism enables a rigorous statistical description of such points. In this paper, we draw inspiration from the statistics of critical points, i.e., points with vanishing gradient (Milnor 1963; Arnold 2006), extending the standard peak constraints (Bardeen et al. 1986) to various topological features in cosmic fields. This approach has not only established cosmological probes (Gay et al. 2012; Moon et al. 2023; Shim et al. 2024), but also provided robust theoretical descriptions for the alignment (Codis et al. 2015), connectivity (Codis et al. 2018; Kraljic et al. 2022), clustering (Shim et al. 2021), and merger history (Cadiou et al. 2020) of the large-scale structures.

Building on this framework, we model halos as high density peaks and filamentary tidal environments as regions that experience contraction along two axes. We evaluate the conditional

* jsshim@pusan.ac.kr

** pogosyan@ualberta.ca

*** myjeon@khu.ac.kr

**** Corresponding author: pichon@iap.fr

PDF of density peaks occurring at a given location under two-dimensional tidal compression. This allows us to identify the preferred relative scale of filaments – the scale ratio between filaments and halos, where filaments most sensitively influence halos. We determine this by locating the inflection point of the conditional PDF, which represents the relative scale of maximum sensitivity where the correlation changes most rapidly.

Our approach offers insights complementary to those presented in Shim et al. (2021), which investigated the clustering of critical points, including peak-to-filament statistics, and derived the characteristic length of filaments connecting clusters. While their analysis examined density peaks and saddles on a single scale at different positions, our analysis considers high-enough density points¹ and potential saddles at the *same* position, but on two *different* scales. By focusing on this local multiscale coupling rather than spatial clustering, our framework allows us to simply identify the characteristic scale ratio at which halos (peaks) most sensitively respond to the surrounding filamentary environment (filament-saddles).

The corresponding scaling laws should prove numerically useful for identifying the size of Lagrangian patches that need to be modeled at high resolution in zoom simulations (Cadiou et al. 2022), while ensuring that the anisotropy of the surrounding environment is properly taken into account. They will also help guide the analysis of observational surveys (Euclid Collaboration et al. 2025; Ivezić et al. 2019; DESI Collaboration et al. 2016), whose mass completeness should be evaluated in relation to the dynamically relevant filamentary scales.

This paper is organized as follows. Section 2 presents the theoretical description of the conditional PDF for two-dimensional tidal compression subject to density peaks occurring on smaller scales. Section 3 presents the main results for a Λ CDM power spectrum, and discusses their local relationship to scale-invariant power spectra, while Section 4 provides conclusions. Details of the derivation for the conditional PDF for two- and three-dimensional GRFs are given in Appendix A. Appendix B presents simplifications in the estimation when power-law power spectra are assumed. The corresponding results in two and three dimensions are given in Appendix C, while comparison to Λ CDM is carried in Appendix D.

2. Predictions: halos in filaments

We consider the probability of having a halo at the Lagrangian scale R_{pk} , determined by the halo mass, in the filamentary environment at scale R_{sd} . We propose a simple model where the presence of the halo is determined by the overdensity value $\delta(R_{\text{pk}})$ exceeding the critical value δ_c , relying on the observation (Kaiser 1984) that high overdensity regions track neighborhoods of density peak. Conversely, the filamentary nature of the region is determined by the signature of the sorted eigenvalues $\lambda_3 < \lambda_2 \leq 0, \lambda_1 \geq 0$ of the deformation tensor $\Psi_{,ij}(R_{\text{sd}})$, *centred at the same position as the halo*, but at the scale R_{sd} ². Here, Ψ is the linear displacement potential of the growing adiabatic mode

¹ We employ high-density regions as statistical proxies for density peaks (Paranjape & Sheth 2012) where halos form (Bardeen et al. 1986). This approach allows for a more tractable analytical treatment of the conditional PDF, while maintaining a physically consistent mapping to the locations of halo formation.

² Throughout this paper, we will use subscripts ‘pk’ and ‘sd’ as a proxy to label high density (‘peak’) and the signature constraint (‘saddle’) respectively.

(Zel’dovich 1970), scaled to satisfy $\Delta\Psi = -\delta$, while $i, j = 1, 2, 3$ designate the spatial derivatives³.

Our primary object of interest is, thus, the conditional probability that the matter flow at scale R_{sd} is compressing along the two axes (as in a filamentary environment), given that the local overdensity δ at a scale R_{pk} exceeds the critical threshold δ_{pk} and represents a collapsed halo. It is given by

$$P(\text{sd|pk}) = \frac{P(\text{sd, pk})}{P(\text{pk})}, \quad (1)$$

where

$$P(\text{sd, pk}) \equiv P(\lambda_2 \leq 0, \lambda_1 \geq 0, \delta \geq \delta_{\text{pk}}) \quad (2)$$

is the joint probability of the deformation tensor and the density field subject to the relevant eigenvalues constraints, and $P(\text{pk}) \equiv P(\delta \geq \delta_{\text{pk}})$ is its marginal.

To evaluate the conditional probability in Equation (1), it is convenient to express the JPDF using the rotational invariants introduced in (Gay et al. 2012) (see Appendix A) that are scaled by their variances. The variance of the density field smoothed on a scale R is given by

$$\sigma_0^2(R) = 4\pi \int dk k^2 P_m(k) W^2(kR), \quad (3)$$

where $P_m(k)$ is the initial power spectrum and $W(kR) = \exp(-k^2 R^2/2)$ is the Gaussian filtering function in k -space with smoothing scale R . The deformation tensor is of the same order of derivatives as the density, and the variance of its trace is also $\langle \Delta\Psi(R_{\text{sd}})^2 \rangle = \sigma_0^2(R_{\text{sd}})$.

Within this formalism, the probability for the local overdensity δ at scale R_{pk} exceeding a critical threshold δ_{pk} , jointly with the condition that the matter flow at scale R_{sd} is compressive along two axes, can be written as follows

$$P(\text{sd, pk}) = \frac{25\sqrt{5}}{12\pi\sqrt{2\pi(1-\gamma^2)}} \int_{\nu_{\text{pk}}}^{\infty} dy \exp\left[-\frac{1}{2}y^2\right] \times \int_0^{\infty} dJ_2 \exp\left[-\frac{5}{2}J_2\right] \int_{-2\sqrt{J_2}}^{\sqrt{J_2}} dJ_1 (J_1^3 - 3J_1J_2 + 2J_2^{3/2}) \exp\left[-\frac{1}{2}\frac{(J_1+\gamma y)^2}{1-\gamma^2}\right], \quad (4)$$

and its marginal

$$P(\text{pk}) = \frac{1}{\sqrt{2\pi}} \int_{\nu_{\text{pk}}}^{\infty} \exp\left(-\frac{y^2}{2}\right) dy. \quad (5)$$

where $\nu_{\text{pk}} \equiv \delta_{\text{pk}}/\sigma_0(R_{\text{pk}})$ is a measure of rarity of a peak with overdensity δ_{pk} at the scale R_{pk} . For a Gaussian density field, a threshold $\nu_{\text{pk}} > 2$ typically corresponds to regions around isolated maxima (Pogosyan et al. 1998), whereas peaks exceeding $\nu_{\text{pk}} > 3$ are extremely rare.⁴

Appendix A provides a rapid derivation of Equation (4), including details about the origin of the boundary of integrations. In Equation (4), γ is the correlation coefficient between densities at the same point in space but smoothed at scales R_{pk} and R_{sd}

$$\gamma(R_{\text{pk}}, R_{\text{sd}}) = \frac{4\pi \int dk k^2 P_m(k) W(kR_{\text{pk}}) W(kR_{\text{sd}})}{\sigma_0(R_{\text{pk}})\sigma_0(R_{\text{sd}})}. \quad (6)$$

³ In the linear regime the displacement potential Ψ is proportional to the gravitational potential ϕ with a negative sign.

⁴ Within a spherical collapse model and standard Λ CDM cosmology, the halo of $M \approx 2 \times 10^{14} h^{-1} M_{\odot}$ that collapses at redshift $z = 0$ corresponds to $\nu_{\text{pk}} \approx 2.1$.

Together with ν_{pk} , which represents the rarity of the peak, γ fully encodes the two physical scales under consideration, and their connections to the properties of the underlying primordial power spectrum. For scale-invariant power spectra, which are a good local proxy to the Λ CDM spectrum when smoothed over a given scale, it becomes a function of the ratio between the two scales, given by Equation (B.1) in Appendix B.

In the next section, we will compute the realm of influence of filament around a given peak as the scale ratio at which the conditional PDF, Equation (1), presents an inflection point as a function of R_{sd} . This is the scale that marks the transition between the volume collapsing along all three axes near the peak to the realm of two-axes collapsing flow.⁵ Note that a more intricate calculation would involve additionally imposing a maximum constraint at the peak scale. This would require higher order derivatives PDFs.

3. Results

3.1. Inflection versus rarity

We study the conditional probability, $P(\text{sd|pk})$, computed using Equation (1), as a function of the scale ratio, $R_{\text{sd}}/R_{\text{pk}}$. This conditional probability quantifies the likelihood that the displacement field smoothed on R_{sd} undergoes two-dimensional compression – forming a filament – given the presence of a density peak – a halo – on a smaller scale R_{pk} . As a starting point, we treat R_{pk} and ν_{pk} as independent parameters, without imposing the condition that the halo has collapsed.

As a practical example, in Figure 1 we consider density peaks above a fixed rarity, ν_{pk} , in a three-dimensional GRF with a Λ CDM power spectrum, smoothed on three different scales. Note that a Gaussian smoothing with a Lagrangian radius of $R_{\text{pk}} = 3.8h^{-1}\text{Mpc}$ produces a density field variance equivalent to that obtained using a tophat smoothing of $8h^{-1}\text{Mpc}$. Thus, we relate the two scale as $R_{\text{pk}} \approx 0.475R_{\text{pk,th}}$. The $P(\text{sd|pk})$ curves are shown for three values of Lagrangian $R_{\text{pk}} = 1.0, 3.8,$ and $9.0h^{-1}\text{Mpc}$, which in Λ CDM model correspond to halo masses of $M = 3.4 \times 10^{12}, 1.8 \times 10^{14}$ and $2.4 \times 10^{15}h^{-1}M_{\odot}$.

The probability $P(\text{sd|pk})$ is suppressed for $R_{\text{sd}} \sim R_{\text{pk}}$, since the vicinity of the peak undergoes collapse along all three directions. It grows to the unconstrained value $(2\sqrt{5} + 3 \tan^{-1} \sqrt{5})/6\pi \approx 0.42$, as $R_{\text{sd}} \gg R_{\text{pk}}$. This value corresponds to the overall fraction of the volume where the filamentary condition is satisfied⁶. We define the inflection point – corresponding to the scale at which the growth rate of $P(\text{sd|pk})$ attains its maximum – as the characteristic scale marking the onset of the filamentary character of the collapse around the peak. At this scale, the exclusion effect associated with the halo constraint is largely alleviated (Shim et al. 2021), whereas the typical overdensity expected within a filament remains significant.

We find that at the inflection point $(R_{\text{sd}}/R_{\text{pk}})_{\text{infl}} \approx 2 - 3$, weakly depending on the peak size R_{pk} . In contrast to scale-invariant power-law spectra cases (see Appendix B), the slope of the power spectrum in the Λ CDM framework steep-

⁵ We could have considered a related definition for this realm of influence. Indeed, nulling the second derivative of Equation (1) with respect to γ will yield some $\gamma_{\text{crit}}(\nu_{\text{pk}})$. Equating this to the $\gamma(R_{\text{pk}}, R_{\text{sd}})$ given by Equation (6) yields an implicit equation for the ratio as a function of ν_{pk} . For two-dimensional fields with power-law spectra, all the calculations can be done explicitly, see Appendix B.

⁶ For some spectra $P(\text{sd|pk})$ may exceed 0.42 at intermediate values of $R_{\text{sd}}/R_{\text{pk}}$.

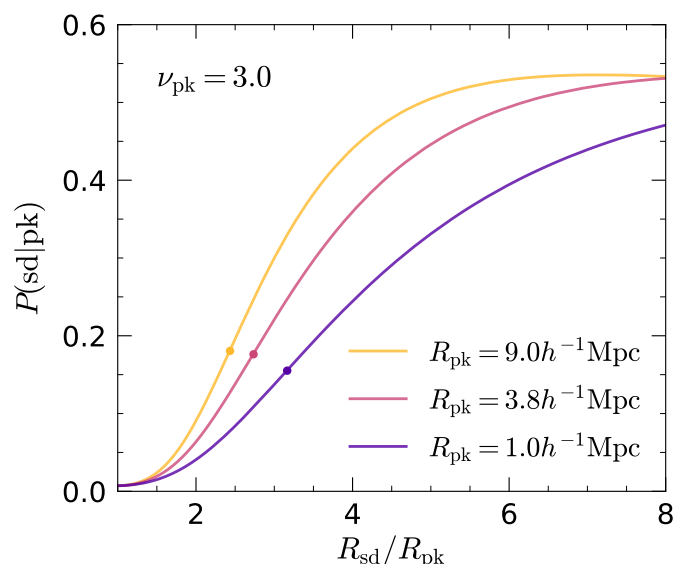


Fig. 1. Conditional probability (from Equation 1) of identifying a filament-saddle tidal structure at scale R_{sd} , given a density peak with $\nu \geq \nu_{\text{pk}} = 3$ at scale R_{pk} , for a three-dimensional GRF with a Λ CDM power spectrum. Solid curves are numerical (Monte-Carlo) results, and filled circles mark the inflection points, tracing the characteristic scale ratio where the halo-filament correlation enhances most significantly. The pink curve corresponds to the tophat filter of $8h^{-1}\text{Mpc}$, which yields $\sigma_8 \approx 0.81$ at $z = 0$.

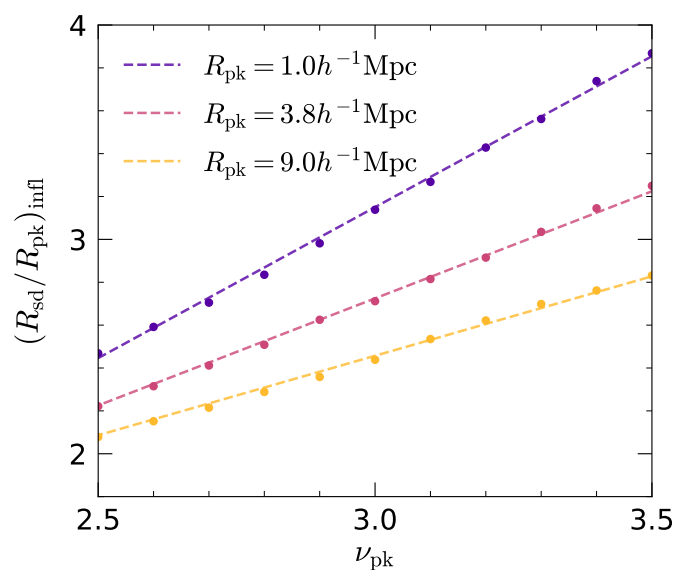


Fig. 2. Characteristic scale ratio as a function of peak rarity for a Λ CDM power spectrum. Dots represent numerical results at the inflection points of conditional PDFs (e.g., Figure 1 for $\nu_{\text{pk}} = 3$), while dashed lines show linear fits. For a rarer peak, halo-filament correlation becomes most sensitive at a larger characteristic scale ratio.

ens toward smaller scales, which leads to larger $(R_{\text{sd}}/R_{\text{pk}})_{\text{infl}}$ for smaller halos.

We now show in Figure 2 how the characteristic scale of filaments, i.e., $(R_{\text{sd}}/R_{\text{pk}})_{\text{infl}}$, depends on peak rarity. We find that it increases monotonically with peak rarity. Typically, we find $2 \leq (R_{\text{sd}}/R_{\text{pk}})_{\text{infl}} < 4$, with higher peaks exhibiting a larger zone of influence and consequently a greater value of $(R_{\text{sd}}/R_{\text{pk}})_{\text{infl}}$.

Conversely, for a fixed peak rarity, the trend of increasing $(R_{\text{sd}}/R_{\text{pk}})_{\text{infl}}$ toward smaller R_{pk} persists across all values of ν_{pk} .

The relation between the peak rarity and the characteristic scale ratio at the inflection points is well described by a linear fit in ν_{pk} ,

$$(R_{\text{sd}}/R_{\text{pk}})_{\text{infl}} = \left(\left[\frac{R_{\text{pk}}}{9.1 \text{Mpc}/h} \right]^2 - \frac{R_{\text{pk}}}{4.9 \text{Mpc}/h} + 1.6 \right) \nu_{\text{pk}} - \left(\left[\frac{R_{\text{pk}}}{6.5 \text{Mpc}/h} \right]^2 - \frac{R_{\text{pk}}}{2.5 \text{Mpc}/h} + 1.45 \right). \quad (7)$$

This linear parameterization reproduces the characteristic scale ratio with an accuracy better than 1% of the measured values for $2.5 \leq \nu_{\text{pk}} < 3.5$ across all three peak sizes examined. As an illustrative example, for peaks identified using Gaussian smoothing with $R_{\text{pk}} = 3.8, h^{-1}\text{Mpc}$ —equivalently, an $8 h^{-1}\text{Mpc}$ tophat smoothing—the direct fit is well described by a practical rule of thumb

$$(R_{\text{sd}}/R_{\text{pk}})_{\text{infl}} \approx 2.2 + (\nu_{\text{pk}} - 2.5), \quad (8)$$

which remains accurate within 1%. This is our first bring-home rule.

3.2. Astrophysical applications

We now examine the filament scales around peaks that have formed collapsed halos. We can then rely on the spherical collapse criterion

$$\nu_{\text{pk}} \sigma_0(R_{\text{pk}}) D(z) = \delta_c, \quad (9)$$

where $D(z)$ is a growing mode of cosmological perturbations, normalized at the present time, $D(0) = 1$, and $\delta_c = 1.686$ is the critical linear overdensity. This condition establishes a relationship between the Lagrangian scale, R_{pk} , and the rarity of a halo, ν_{pk} , and redshift z .

3.2.1. R_{sd} of collapsed objects versus mass and redshift

Let us first focus on $R_{\text{sd}}/R_{\text{pk}}$ as a function of collapsing halo size at fixed redshift. For a ΛCDM spectrum, Equations (3) and (9) define the relationship

$$\nu_{\text{pk}}(R_{\text{pk}}, z) \approx \frac{0.8}{D(z)\sigma_8} \left(\left[\frac{R_{\text{pk}}}{5.15 \text{Mpc}/h} \right]^{\frac{1}{4}} + \frac{R_{\text{pk}}}{3.14 \text{Mpc}/h} \right), \quad (10)$$

in the range of R_{pk} from 0.1 to 10 $h^{-1}\text{Mpc}$ that covers six orders of magnitude in mass from $M \approx 3.3 \times 10^9$ to $M \approx 3.3 \times 10^{15} h^{-1} M_{\odot}$. Conversely, the Gaussian Lagrangian scale of a halo is determined by its mass

$$R_{\text{pk}} \approx 3.1 M_{14}^{1/3} h^{-1} \text{Mpc}, \quad (11)$$

where $M_X = M/(10^X (\Omega_m/0.3) h^{-1} M_{\odot})$. Substituting Equation (10) into Equation (7) gives the relative filamentary scales $R_{\text{sd}}/R_{\text{pk}}$ as a function of R_{pk} for collapsed halos at different redshifts.

Figure 3 presents these curves for $z = 0, 1, 2$ in a ΛCDM universe with $\sigma_8 = 0.81$.⁷ We observe a significant change in

⁷ We set the condition $1.7 < \nu_{\text{pk}} < 3.5$, the range where the high-field value is still a good approximation for the peak condition, but the peaks are not exceedingly rare. This defines the redshift dependent range of scales under consideration. At $z = 0$ the covered range for halo Lagrangian size is, thus, $R_{\text{pk}} \approx 2.8\text{--}7.5 h^{-1}\text{Mpc}$, corresponding to $M \approx 7 \times 10^{13}\text{--}1.4 \times 10^{15} h^{-1} M_{\odot}$.

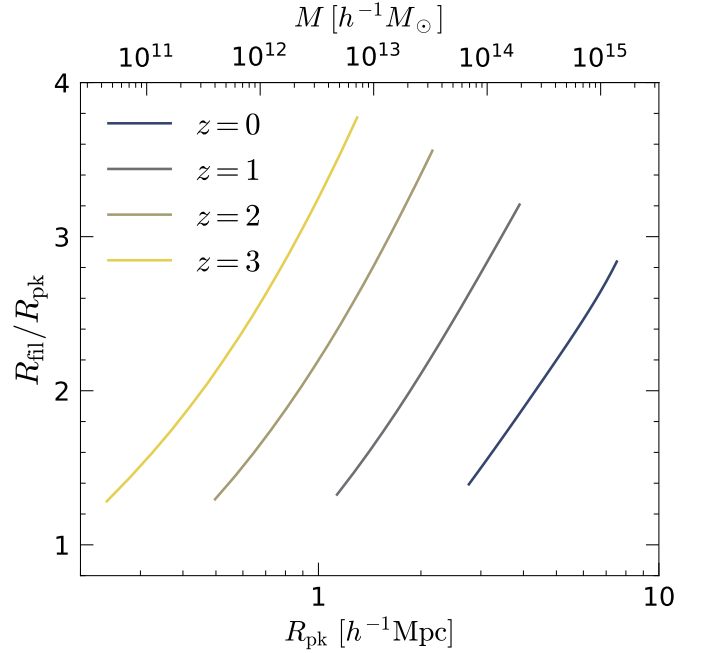


Fig. 3. Characteristic filamentary scale ratio around halos on various scales that collapsed at various redshifts. Halo masses (top x -axis) corresponding to the peak scales (bottom x -axis) are also marked.

the relative filament scale with increasing mass, which can be explained by the transition from abundant low-mass halos to rare high-mass ones. The tendency is even more pronounced at high redshifts where the slope of the power spectrum is steeper in the relevant range of scales. In the range of relevant scales, the curves in Figure 3 can be fitted by simple power-laws⁸

$$(R_{\text{fil}}/R_{\text{pk}}) \approx (R_{\text{pk}}/1.6 h^{-1} \text{Mpc})^{0.68} \quad \text{for } z = 0, \quad (12a)$$

$$(R_{\text{fil}}/R_{\text{pk}}) \approx (R_{\text{pk}}/0.67 h^{-1} \text{Mpc})^{0.68} \quad \text{for } z = 1, \quad (12b)$$

$$(R_{\text{fil}}/R_{\text{pk}}) \approx (R_{\text{pk}}/0.32 h^{-1} \text{Mpc})^{0.68} \quad \text{for } z = 2, \quad (12c)$$

$$(R_{\text{fil}}/R_{\text{pk}}) \approx (R_{\text{pk}}/0.15 h^{-1} \text{Mpc})^{0.62} \quad \text{for } z = 3, \quad (12d)$$

or, using mass in place of R_{pk} from Equation (11),

$$R_{\text{fil}}(M) \approx 4.9 M_{14}^{0.56} h^{-1} \text{Mpc} \quad \text{for } z = 0, \quad (13a)$$

$$R_{\text{fil}}(M) \approx 2.4 M_{13}^{0.56} h^{-1} \text{Mpc} \quad \text{for } z = 1, \quad (13b)$$

$$R_{\text{fil}}(M) \approx 1.1 M_{12}^{0.56} h^{-1} \text{Mpc} \quad \text{for } z = 2, \quad (13c)$$

$$R_{\text{fil}}(M) \approx 0.49 M_{11}^{0.54} h^{-1} \text{Mpc} \quad \text{for } z = 3. \quad (13d)$$

More generally, for arbitrary redshifts, substituting Equation (11) into Equations (10) and (7) allows us to simply compute $R_{\text{fil}}(M, z)$. This is our second bring-home rule.

3.2.2. The environment of the most prominent halos

We now consider the redshift evolution of the characteristic scale of filaments associated with the formation of the largest halos at each redshift. Thus, we fix the halo rarity ν_{pk} threshold at a high value, find from the collapse condition in Equation (9) the Lagrangian size of such halos as a function of the redshift, $R_{\text{pk}}(z)$,

⁸ Note that the power index in the fit corresponds to $(n_{\text{eff}} + 3)/2 \approx 0.68$ for an effective slope of the power spectrum, $n_{\text{eff}} \approx -1.6$ at $3.8 h^{-1}\text{Mpc}$ (see Figure D.1 in Appendix D).

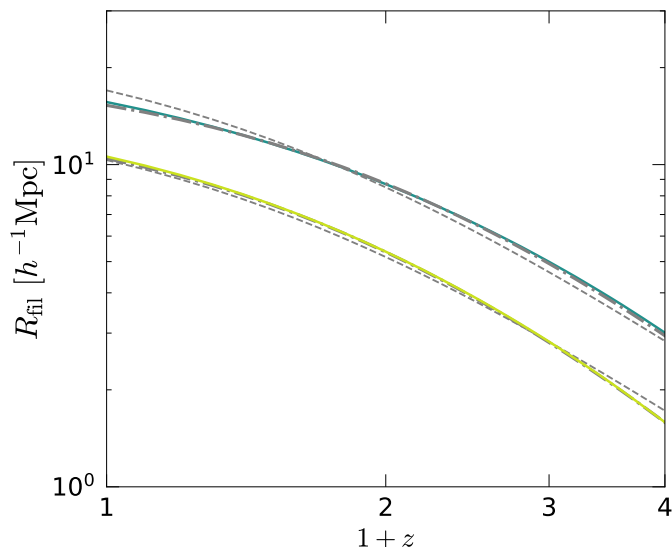


Fig. 4. Characteristic scale of the filamentary tidal environment that most strongly influences density peaks at the time of their collapse, as given by Equation (7). Results are shown for peaks with $\nu_{\text{pk}} = 3.0$ and 2.5 (solid lines), together with their corresponding fits (dashed lines from Equation (14) and dash-dotted lines from Equation (D.4)). This relation identifies the characteristic filament scale that governs the formation of the most massive halos at their epoch of formation.

and, subsequently, determine the $R_{\text{sd}}(z)$ for these $R_{\text{pk}}(z)$ using Equation (7).

In Figure 4, we consider $\nu_{\text{pk}} = 2.5$ and 3.0 density peaks that have reached the spherical collapse threshold density at various epochs, representing some of the most massive halos that formed at any given redshift. For $\nu_{\text{pk}} = 2.5$, these rarest halos typically have masses of $M \approx 3.9 \times 10^{14}, 4.1 \times 10^{13}, 5.3 \times 10^{12}$ and $1.8 \times 10^{11} h^{-1} M_{\odot}$, at $z = 0, 1, 2$ and 4 respectively.

The characteristic scale of filaments increases toward the present day, reflecting the hierarchical assembly of cosmic structures. As more massive halos form at later epochs, the filaments associated with them correspondingly grow larger. This main trend is complemented by the change of the effective slope of the power spectrum at the progressively increasing scale of collapsing objects. We find that the overall trend is well captured with the following simple fit,

$$R_{\text{fil}} [h^{-1} \text{Mpc}] = \begin{cases} \frac{31}{2 + (1+z)^2} & \text{for } \nu_{\text{pk}} = 2.5, \\ \frac{51}{2 + (1+z)^2} & \text{for } \nu_{\text{pk}} = 3.0, \end{cases} \quad (14)$$

which remains accurate within 10% at least up to $z \approx 3$. This is our third bring-home rule. We also provide a more sophisticated theoretically-motivated fitting form in Appendix D, which maintains better accuracy.

3.2.3. Mapping Lagrangian to Eulerian scales

Let us translate our findings into a procedure to optimally smooth observational surveys so as to preserve the dynamically relevant cosmic environment around a given halo. For a halo of a given Lagrangian scale, R_{pk} (resp. mass, M), we can apply the procedure described below Equation (13) to compute the corresponding Lagrangian scale, $R_{\text{fil}}(M, z)$. Conversely, for a halo of a given rarity, we should turn to Equation (14). We suggest that

the corresponding smoothing scale in Eulerian space should be chosen to be $R_{\text{fil,Eulerian}} \equiv R_{\text{fil,Lagrangian}}$, because filaments lie in mildly nonlinear regime, where the difference between the Lagrangian and Eulerian scales is not significant.⁹

4. Conclusion

We investigated whether a characteristic scale exists at which filamentary environments most strongly influence the formation of halos and galaxies. To this end, we analyzed the conditional probability distribution function of the density of potential saddles – that delineate filamentary environments, conditioned to the density peaks – tracers of halos. We defined the characteristic scale ratio $(R_{\text{sd}}/R_{\text{pk}})_{\text{inff}}$ between these density and tidal structures as the inflection point of the conditional PDF, marking the regime where the halo– filament correlation is maximally sensitive to variations in the filament scale.

Our results show that, although the strength of the halo– filament correlation increases monotonically with the scale ratio, its sensitivity reaches a maximum at a specific value dependent on both the rarity, ν_{pk} , and the scale, R_{pk} , of the density peak. This implies that the *effective* filamentary environment does not correspond to a fixed, universal scale but is closely tied to the peak’s scale and rarity—that is, to halo mass. Our findings for the three-dimensional Λ CDM power spectrum are consistent with those obtained for power-law spectra (see Appendix C.2) and remain robust in the two-dimensional analyses where analytical predictions are available (see Appendix C.1).

Our findings are therefore summarized as follows: the characteristic scale ratio which halo formation responds most sensitively to filaments varies with halo scale (i.e., size and rarity of a peak), following Equation (7); the linear scaling establishes the zone of anisotropic influence on collapsing halos, typically extending to 2–3 times the size of their Lagrangian patch; the typical filament scale one should consider as a function of peak scale or mass and redshift is given by Equations (12) and (13); the characteristic filament scale evolves with redshift and is well approximated by Equation (14).

These findings offer practical guidance for identifying the characteristic scales of filamentary structures in galaxy evolution studies. The derived scaling relations provide a framework for selecting optimal smoothing lengths in survey analyses on the one hand (Laigle et al. 2025), and for defining the initial patch sizes in zoom-in simulations (Buehlmann et al. 2025), ensuring that the relevant filamentary environment is accurately captured on the other hand.

Indeed, our result offers a quantitative improvement over the usual practice of choosing buffer regions in zoom simulations by trial and error or purely based on spherical overdensity arguments, and it provides a clean way to control systematics in studies of spin alignment, shape, and merger histories driven by anisotropic infall.

Conversely, in large surveys such as Euclid, LSST, or DESI (Euclid Collaboration et al. 2025; Ivezić et al. 2019; DESI Collaboration et al. 2016), one can tune multiscale filament finders so that the smoothing length used to define filaments corresponds to the dynamically relevant scale inferred for the haloes and galaxies under study, rather than adopting a one-size-fits-all scale. In such observational settings one usually deals with Eulerian scales. When one deals with relatively

⁹ For instance, focusing on $10^{14} h^{-1} M_{\odot}$ halos in a vanilla Λ CDM universe at $z = 0$, Equation (13) states that the large scales structures should be smoothed over a $R_{\text{fil,Eulerian}} = 4.9 h^{-1} \text{Mpc}$ Gaussian filter.

rare halos, these scales are in mildly nonlinear regime, where the Lagrangian and Eulerian scales are similar. So our recipe is to determine the scale of the peaks from their mass, and using R_{sd} in Eulerian space. This is especially important when interpreting environmental trends in galaxy properties (e.g. colour, morphology, or star formation) as a function of distance to filaments, since the “right” filament scale depends on halo rarity and evolves with redshift.

Acknowledgements

We thank Corentin Cadiou, Simon Prunet, Ho Seong Hwang, Katarina Kraljic and Sabri Errachdi for useful discussions. JS acknowledges the support by Academia Sinica Institute of Astronomy and Astrophysics. M.-J. is supported by Samsung Science and Technology Foundation under Project Number SSTF-BA2402-03. This work is partially supported by the grant GALBAR ANR-25-CE31-4684 and IDF-DIM-ORIGINES-2023-4-11, and from the CNRS through the MITI interdisciplinary programs.

References

- Aragón-Calvo, M. A., van de Weygaert, R., Jones, B. J. T., & van der Hulst, J. M. 2007, *ApJ*, **655**, L5
- Arnold, V. I. 2006, Ordinary differential equations (Berlin, Germany New York: Springer)
- Arora, A., Garavito-Camargo, N., Sanderson, R. E., et al. 2025, *ApJ*, **988**, 190
- Bardeen, J. M., Bond, J. R., Kaiser, N., & Szalay, A. S. 1986, *ApJ*, **304**, 15
- Bond, J. R., Cole, S., Efstathiou, G., & Kaiser, N. 1991, *ApJ*, **379**, 440
- Bond, J. R., Kofman, L., & Pogosyan, D. 1996, *Nature*, **380**, 603
- Borzyszkowski, M., Porciani, C., Romano-Díaz, E., & Garaldi, E. 2017, *MNRAS*, **469**, 594
- Buehlmann, M., Winkler, L., Hahn, O., Helly, J. C., & Jenkins, A. 2025, *The Open Journal of Astrophysics*, **8**
- Cadiou, C., Dubois, Y., & Pichon, C. 2022, *MNRAS*, **514**, 5429
- Cadiou, C., Pichon, C., Codis, S., et al. 2020, *MNRAS*, **496**, 4787
- Codis, S., Pichon, C., Devriendt, J., et al. 2012, *MNRAS*, **427**, 3320
- Codis, S., Pichon, C., & Pogosyan, D. 2015, *MNRAS*, **452**, 3369
- Codis, S., Pogosyan, D., & Pichon, C. 2018, *MNRAS*, **479**, 973
- de Lapparent, V., Geller, M. J., & Huchra, J. P. 1986, *ApJ*, **302**, L1
- DESI Collaboration, Aghamousa, A., Aguilar, J., et al. 2016, *arXiv e-prints*, [arXiv:1611.00036](https://arxiv.org/abs/1611.00036)
- Euclid Collaboration, Mellier, Y., Abdurro’uf, et al. 2025, *A&A*, **697**, A1
- Gay, C., Pichon, C., & Pogosyan, D. 2012, *Phys. Rev. D*, **85**, 023011
- Hahn, O., Carollo, C. M., Porciani, C., & Dekel, A. 2007, *MNRAS*, **381**, 41
- Hahn, O., Porciani, C., Dekel, A., & Carollo, C. M. 2009, *MNRAS*, **398**, 1742
- Ivezić, Ž., Kahn, S. M., Tyson, J. A., et al. 2019, *ApJ*, **873**, 111
- Jhee, H., Song, H., Smith, R., et al. 2022, *ApJ*, **940**, 2
- Kaiser, N. 1984, *ApJ*, **284**, L9
- Klypin, A. & Shandarin, S. F. 1993, *ApJ*, **413**, 48
- Kraljic, K., Arnouts, S., Pichon, C., et al. 2018, *MNRAS*, **474**, 547
- Kraljic, K., Laigle, C., Pichon, C., et al. 2022, *MNRAS*, **514**, 1359
- Kraljic, K., Pichon, C., Codis, S., et al. 2020, *MNRAS*, **491**, 4294
- Kraljic, K., Pichon, C., Dubois, Y., et al. 2019, *MNRAS*, **483**, 3227
- Laigle, C., Pichon, C., Arnouts, S., et al. 2018, *MNRAS*, **474**, 5437
- Laigle, C., Pichon, C., Codis, S., et al. 2015, *MNRAS*, **446**, 2744
- Laigle, E. C. C., Gouin, C., Sarron, F., et al. 2025, Euclid Quick Data Release (Q1). Galaxy shapes and alignments in the cosmic web
- Lee, Y., Kim, S., Rey, S.-C., & Chung, J. 2021, *ApJ*, **906**, 68
- Libeskind, N. I., Hoffman, Y., Knebe, A., et al. 2012, *MNRAS*, **421**, L137
- Milnor, J. 1963, Morse theory (Princeton, NJ: Princeton University Press)
- Moon, J., Rossi, G., & Yu, H. 2023, *ApJS*, **264**, 26
- Musso, M., Cadiou, C., Pichon, C., et al. 2018, *MNRAS*, **476**, 4877
- Paranjape, A. & Sheth, R. K. 2012, *MNRAS*, **426**, 2789
- Pogosyan, D., Bond, J. R., Kofman, L., & Wadsley, J. 1998, in Wide Field Surveys in Cosmology, ed. Colombi, S., Mellier, Y., & Raban, B., Vol. 14, **61**
- Shim, J., Codis, S., Pichon, C., Pogosyan, D., & Cadiou, C. 2021, *MNRAS*, **502**, 3885
- Shim, J. & Lee, J. 2018, *arXiv e-prints*, [arXiv:1801.09960](https://arxiv.org/abs/1801.09960)
- Shim, J., Lee, J., & Hoyle, F. 2015, *ApJ*, **815**, 107
- Shim, J., Pichon, C., Pogosyan, D., et al. 2024, *MNRAS*, **528**, 1604
- Song, H., Laigle, C., Hwang, H. S., et al. 2021, *MNRAS*, **501**, 4635
- Sousbie, T. 2011, *MNRAS*, **414**, 350
- Sousbie, T., Pichon, C., Colombi, S., Novikov, D., & Pogosyan, D. 2008, *MNRAS*, **383**, 1655
- Tojeiro, R., Eardley, E., Peacock, J. A., et al. 2017, *MNRAS*, **470**, 3720
- Yu, G., Zhu, W., Yang, Q.-R., et al. 2025, *ApJ*, **986**, 193
- Zel’dovich, Y. B. 1970, *A&A*, **5**, 84

Appendix A: Rotational invariants and PDFs

Here we present the Gaussian joint probability distribution function (JPDF) of the (scaled) deformation tensor and the density, defined at the same point in space, but at different scales.

Appendix A.1: Rotational invariants in 3D

It is convenient to write the JPDF of the relevant quantities using variables normalized by the density variance, $x_{ij} = \Psi_{ij}/\sigma_0(R_{sd})$ and $y = \delta/\sigma_0(R_{pk})$. The JPDF then has a similar formal structure

$$P(x_{ij}, y) dx_{ij} dy, \quad (\text{A.1})$$

as the JPDF of the field and its derivatives studied in (Gay et al. 2012). The only difference is that in (Gay et al. 2012) x_{ij} represented the normalized version of the Hessian of the density, and here it is the deformation tensor. Both the density Hessian and deformation tensor eigenvalues have the same filamentary condition $\lambda_3 \leq \lambda_2 < 0, \lambda_1 > 0$, and both are negatively correlated with the density, $\langle \text{Tr}(x_{ij})\delta \rangle = -\gamma$. Correspondingly, in (Gay et al. 2012) γ represents the correlation between density and its Laplacian at the same scale, whereas in this paper it represents the density correlation at different scales but at the same point. We are once again interested in statistical measures that are rotation-invariant at arbitrary points in space. Therefore, the results of (Gay et al. 2012), including the development of non-Gaussian corrections, can be directly applied in the present work.

Following (Gay et al. 2012), we introduce polynomial in field rotational invariants that describe our problem: the density value y itself and the invariants of the second rank matrix x_{ij} .

$$I_1 \equiv \text{Tr}(x_{ij}) = x_{11} + x_{22} + x_{33}, \quad (\text{A.2a})$$

$$I_2 \equiv x_{11}x_{22} + x_{22}x_{33} + x_{11}x_{33} - x_{12}^2 - x_{23}^2 - x_{13}^2, \quad (\text{A.2b})$$

$$I_3 \equiv \det|x_{ij}| = x_{11}x_{22}x_{33} + 2x_{12}x_{23}x_{13} - x_{11}x_{23}^2 - x_{22}x_{13}^2 - x_{33}x_{12}^2. \quad (\text{A.2c})$$

The same invariants expressed through eigenvalues are

$$I_1 = \lambda_1 + \lambda_2 + \lambda_3, \quad I_2 = \lambda_1\lambda_2 + \lambda_2\lambda_3 + \lambda_1\lambda_3, \quad I_3 = \lambda_1\lambda_2\lambda_3.$$

These variables can be made partially independent using the linear combinations

$$J_1 = I_1, \quad J_2 = I_1^2 - 3I_2 \quad \text{and} \quad J_3 = I_1^3 - \frac{9}{2}I_1I_2 + \frac{27}{2}I_3,$$

which with our normalization have the following lowest (up to quadratic in the field variables) moments

$$\langle y \rangle = 0, \quad \langle J_1 \rangle = 0, \quad \langle y^2 \rangle = 1, \quad \langle J_1^2 \rangle = 1, \quad \langle J_2 \rangle = 1,$$

and the only non-vanishing cross-correlation

$$\langle yJ_1 \rangle = -\gamma(R_{pk}, R_{sd}), \quad (\text{A.3})$$

where $\gamma(R_{pk}, R_{sd})$ is the correlation coefficient between densities at the same point in space but smoothed at scales R_{pk} and R_{sd} given by Equation (6). Clearly, $\gamma(R, R) = 1$. In terms of these variables, the Gaussian JPDF is given by

$$G_{3D}(y, J_1, J_2, J_3) = \frac{25\sqrt{5} \exp\left[-\frac{1}{2} \frac{y^2 + 2\gamma y J_1 + J_1^2}{1 - \gamma^2} - \frac{5J_2}{2}\right]}{12\pi\sqrt{2\pi(1 - \gamma^2)}},$$

with J_3 distributed uniformly between $-J_2^{3/2}$ and $J_2^{3/2}$.

Then, by definition, $P(\text{sd}, \text{pk})$ reads

$$P(\text{sd}, \text{pk}) \equiv \langle \theta(-\lambda_2)\theta(\lambda_2 - \lambda_3)\theta(\lambda_1)\theta(y - \nu_{pk}) \rangle, \quad (\text{A.4})$$

requiring the flow to be compressive along two axes and the peak density contrast to be above the threshold ν_{pk} . In Equation (A.4), the expectation is evaluated using the Gaussian JPDF G_{3D} , while θ is the Heaviside function. The filamentary domain for the deformation tensor, expressed in terms of the J_i variables, (see, e.g. Gay et al. 2012) reads $J_2 \in [0, \infty[$, $J_1 \in [-2J_2^{1/2}, J_2^{1/2}]$ and $J_3 \in [-\frac{1}{2}J_1^3 + \frac{3}{2}J_1J_2, J_2^{3/2}]$. Hence

$$P(\text{sd}, \text{pk}) = \int_{\nu_{pk}}^{\infty} dy \int_0^{\infty} dJ_2 \int_{-2J_2^{1/2}}^{J_2^{1/2}} dJ_1 \int_{-\frac{1}{2}J_1^3 + \frac{3}{2}J_1J_2}^{J_2^{3/2}} dJ_3 G_{3D},$$

leading to Equation (4) in the main text after integration over J_3 .¹⁰

Appendix A.2: Rotational invariants in 2D

The rotation invariant formalism is straightforwardly adapted to 2D random fields, which are of interest for e.g. CMB, intensity maps and weak lensing studies. There are just two polynomial invariants that describe the deformation tensor in 2D,

$$I_1 \equiv \text{Tr}(x_{ij}) = x_{11} + x_{22} \quad \text{and} \quad I_2 \equiv \det|x_{ij}| = x_{11}x_{22} - x_{12}^2$$

expressed via eigenvalues as

$$I_1 \equiv \text{Tr}(x_{ij}) = \lambda_1 + \lambda_2, \quad \text{and} \quad I_2 \equiv \det|x_{ij}| = \lambda_1\lambda_2.$$

We shall also use the orthogonal set

$$J_1 = I_1, \quad \text{and} \quad J_2 = I_1^2 - 4I_2 = (x_{11} - x_{22})^2 + 4x_{12}^2.$$

We can then express the 2D Gaussian JPDF including the field value, y , normalized over $dydJ_1dJ_2$ as

$$G_{2D}(y, J_1, J_2) = \frac{\exp\left[-\frac{1}{2} \frac{y^2 + 2\gamma y J_1 + J_1^2}{1 - \gamma^2} - J_2\right]}{2\pi\sqrt{1 - \gamma^2}}. \quad (\text{A.5})$$

The integration domain associated with the saddle condition in the velocity potential field is defined by (Gay et al. 2012) as $J_1 \in [-\infty, \infty]$, $J_2 \in [J_1^2, \infty]$, with the rarity condition, $y \geq \nu_{pk}$. In contrast to 3D case, the integration in Equation (A.5) over J_1 , J_2 , and y can be done analytically, and yields

$$P_{2D}(\text{sd}, \text{pk}) \equiv \langle \theta(-\lambda_2)\theta(\lambda_1)\theta(y - \nu_{pk}) \rangle = \frac{1}{2\sqrt{3}} \text{erfc}\left(\frac{\sqrt{3}\nu_{pk}}{\sqrt{6 - 4\gamma^2}}\right),$$

with the marginal

$$P(\text{pk}) = \frac{1}{2} \text{erfc}\left(\frac{\nu_{pk}}{\sqrt{2}}\right), \quad (\text{A.6})$$

which allows us to finally write the conditional PDF in the final purely analytic form

$$P_{2D}(\text{sd}|\text{pk}) = \frac{P_{2D}(\text{sd}, \text{pk})}{P(\text{pk})} = \frac{1}{\sqrt{3}} \frac{\text{erfc}\left(\frac{\sqrt{3}\nu_{pk}}{\sqrt{6 - 4\gamma^2}}\right)}{\text{erfc}\left(\frac{\nu_{pk}}{\sqrt{2}}\right)}. \quad (\text{A.7})$$

¹⁰ The integral over J_1 can also be performed analytically, although the resulting expression is rather cumbersome.

Appendix B: Power-law spectra

In this and the following two appendices, we perform validity tests of our numerical calculations, using scale-invariant power-law spectra, $P_m(k) \propto k^n$. For such spectra $\sigma_0(R) \sim R^{-\frac{n+d}{2}}$ and the correlation coefficient in Equation (6) becomes a simple function of two variables – the scale ratio $R_{\text{sd}}/R_{\text{pk}}$ and spectral index n given by

$$\gamma(R_{\text{sd}}, R_{\text{pk}}) = \left(\frac{2(R_{\text{sd}}/R_{\text{pk}})}{1 + (R_{\text{sd}}/R_{\text{pk}})^2} \right)^{\frac{n+d}{2}}, \quad (\text{B.1})$$

where d is the dimension of the space and $n > -d$.

For the power law spectrum, $\gamma(R_{\text{sd}}, R_{\text{pk}})$ clearly depends only on the ratio $R_{\text{sd}}/R_{\text{pk}}$. As the result, any characteristic scale R_{sd} of the probability distribution $P(\text{sd}|\text{pk})$ (treated as an implicit function of R_{sd} via γ) corresponds to some characteristic value, γ_*

$$\gamma(R_{\text{sd}}/R_{\text{pk}}) = \gamma_*(\nu_{\text{pk}}, n, d) \quad (\text{B.2})$$

that does not depend on R_{pk} . Then, the γ_* corresponding to the inflection point, $d^2 P(\text{sd}|\nu_{\text{pk}})/dR_{\text{sd}}^2 = 0$, is defined implicitly by the equation

$$\gamma \frac{d^2 P}{d^2 \gamma} + \frac{dP}{d\gamma} \left(1 - \frac{\gamma^{\frac{4}{n+d}} - \sqrt{1 - \gamma^{\frac{4}{n+d}}}}{\frac{n+d}{2} (1 - \gamma^{\frac{4}{n+d}})} \right) = 0. \quad (\text{B.3})$$

Once γ_* is identified, inverting Equation (B.2) for the scale ratio gives

$$R_{\text{sd}}/R_{\text{pk}} = \gamma_*^{-\frac{2}{n+d}} \left(1 + \sqrt{1 - \gamma_*^{\frac{4}{n+d}}} \right). \quad (\text{B.4})$$

For instance, for 2D scale invariant spectra and $\nu_{\text{pk}} = 2.5$, we find, via Equations (B.3) and (B.4), and given the analytical Equation (A.7) for $P(\text{sd}|\text{pk})$, $\gamma_* \approx 0.79, 0.73, 0.69$ and $R_{\text{sd}}/R_{\text{pk}} \approx 4.8, 3.5, 2.9$ for $n = -1.5, -1, -0.5$ respectively. The R_{sd} scale raises up to $R_{\text{sd}}/R_{\text{pk}} \approx 7.1, 4.5, 3.5$ in the environment of rare peaks, $\nu_{\text{pk}} = 3$.

In Appendix C we present the 2D and 3D GRF power-law cases, and compare the 3D case to the Λ CDM model presented in the main text in Appendix D.

Appendix C: Power-law spectra zone of influence

Let us present here the zone of influence of peaks in scale-invariant Gaussian random fields, for which analytical results are available in 2D.

Appendix C.1: 2D Power-law spectra

We first show in Figure C.1 the conditional probability, $P(\text{sd}|\text{pk})$, for power-law spectra, $P(k) \propto k^n$, and at fixed $\nu_{\text{pk}} = 2.5$. Our numerical calculations are in full agreement with the analytical predictions of Appendix B. Similarly to Figure 1, we observe that the probability increases with the scale ratio, approaching a nearly constant value at very large $R_{\text{sd}}/R_{\text{pk}}$. For example, for $n = -0.5$, the conditional probability saturates at around $R_{\text{sd}}/R_{\text{pk}} \approx 30$, earlier than for the $n = -1$ and -1.5 cases. We also find a notable dependence on the spectral index of the power spectrum. At a fixed scale ratio, the probability becomes smaller for a power spectrum with more negative index, implying higher

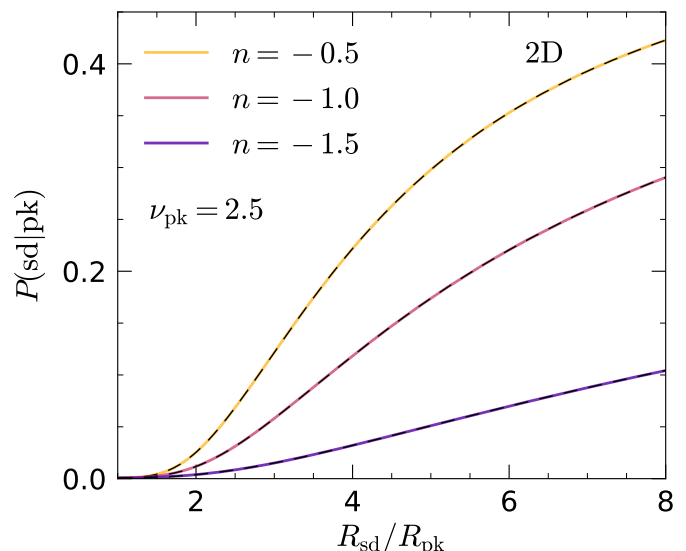


Fig. C.1. Similar to Figure 1, but for $\nu_{\text{pk}} = 2.5$ in a two-dimensional GRF, computed using Equation (A.7), with a power-law spectrum, $P_m(k) \propto k^n$. Solid curves show numerical results, whereas black dashed curves show analytical predictions.

suppression of filamentary behaviour near the peaks¹¹. This is due to the greater influence of long-wavelength modes, whose large-scale effects increase the likelihood that the surroundings of the peak will collapse simultaneously along all axes.

In Figure C.2, we display the dependence of the inflection point of the conditional PDF, $P(\text{sd}|\text{pk})$, on peak rarity for the power spectrum with $n = -1$. Here we consider a wide rarity range, since the minimum rarity threshold for peak formation is slightly smaller in two dimensions than in the three-dimensional case. The top panel indicates that, for a fixed peak size, higher density peaks are less likely to reside within the filamentary environments of the tidal field. This suggests that the conditions required for peak formation and two-dimensional compression become increasingly incompatible as peak rarity increases. Consequently, for more prominent peaks to achieve a comparable level of peak-saddle correlation, the tidal structures must be defined on significantly larger scales. In the bottom panel, inflection points are identified as maxima of the derivative. A clear trend emerges: the inflection point – the location of highest sensitivity – shifts toward larger scale ratios as the peak rarity increases.

Finally, Figure C.3 summarizes the increasing trend of filamentary scale with peak rarity in two dimensions. Our numerical results are in agreement with the analytical predictions. Interestingly, the relationship between the scale ratio and peak rarity becomes increasingly linear for higher spectral indices (e.g., $n \approx 0$), whereas it gradually transitions to a power-law behavior as the index approaches the negative of the spatial dimension (i.e., $n \sim -d$).

¹¹ Unlike the 3D case, where two distinct types of saddle points exist (including filament-type saddles), only a single class of saddles occurs in 2D. We nonetheless describe a region as *filamentary* if it collapses along one axis while expanding along the other. In two dimensions, such regions may be either over- or underdense. We therefore do not impose a positive overdensity constraint, which allows the 2D case to be treated on the same footing as the 3D one. By contrast, in 3D, filamentary regions are generally overdense even without such an explicit constraint.

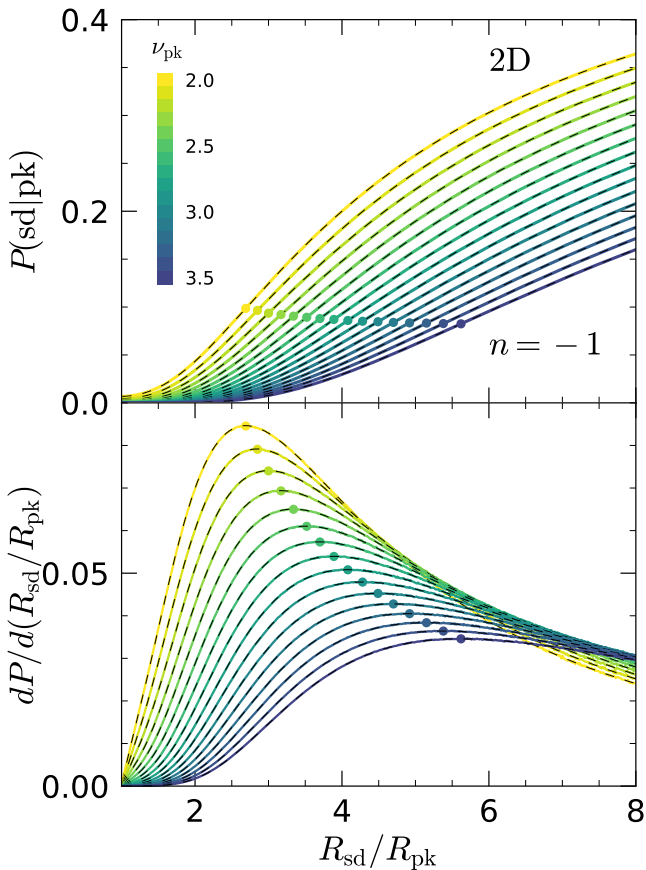


Fig. C.2. Conditional probability (top) and its derivative (bottom) for a 2D GRF with power spectrum, $P_m(k) \propto k^{-1}$, computed using Equation (A.7). Solid curves are numerical results, and black dashed curves show analytic predictions, for 15 equally-spaced ν_{pk} as labeled. Inflection points (filled circles) are identified as maxima of the derivatives of $P(\text{sd}|\text{pk})$ with respect to the scale ratio.

Appendix C.2: 3D Power-Law spectra

Building on the consistency between the numerical and analytical results in two dimensions, we now extend our investigation to three dimensions, where the derivation lacks a closed-form solution. Figure C.4 displays the numerically calculated conditional probabilities for power-law spectra in three dimensions. Overall, the three-dimensional results align well with the two-dimensional trends: the halo-filament correlation strengthens with an increasing scale ratio, while it weakens as the spectral index becomes more negative.

The peak rarity dependence of the conditional probability in three dimensions, shown in Figure C.5, follows a trend analogous to the results for two dimensions presented in Figure C.2. Specifically, for a fixed scale ratio, the halo-filament correlation weakens as peaks become more prominent. As shown in the lower panel, the characteristic scale ratio (defined by the apsis of the inflection point) shifts toward larger values for higher peaks. This trend reinforces the earlier established scaling relation, confirming that more massive halos are most sensitively associated with an even larger filamentary environment. We again show the relation between the characteristic scale ratio and peak rarity in Figure C.6. As for the three-dimensional Λ CDM power spectrum, we employ a linear fit calibrated for $\nu_{\text{pk}} \geq 3$, which provides a very good match to the numerical results. This linear fit remains valid even when extended to lower-rarities, except

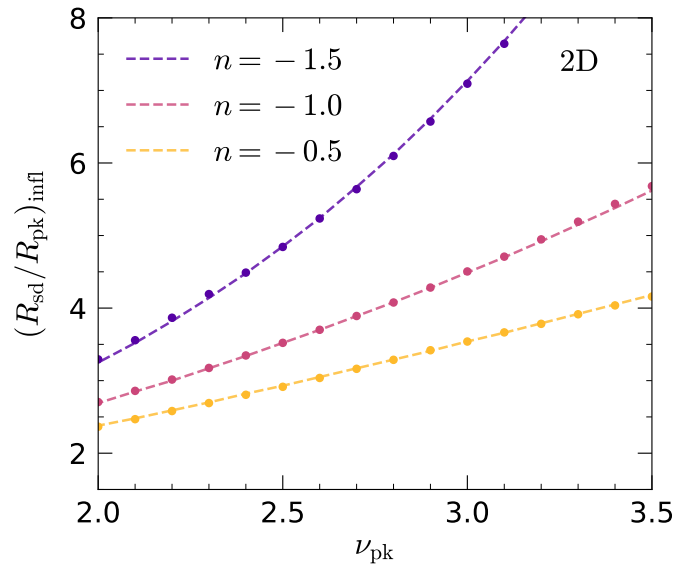


Fig. C.3. Similar to Figure 2, but for peaks and saddles in a 2D GRF with power-law power spectra. Dotted lines represent numerical results, while dashed lines show analytical predictions. The peak-saddle correlation becomes most sensitive at larger scale ratios for rarer peaks.

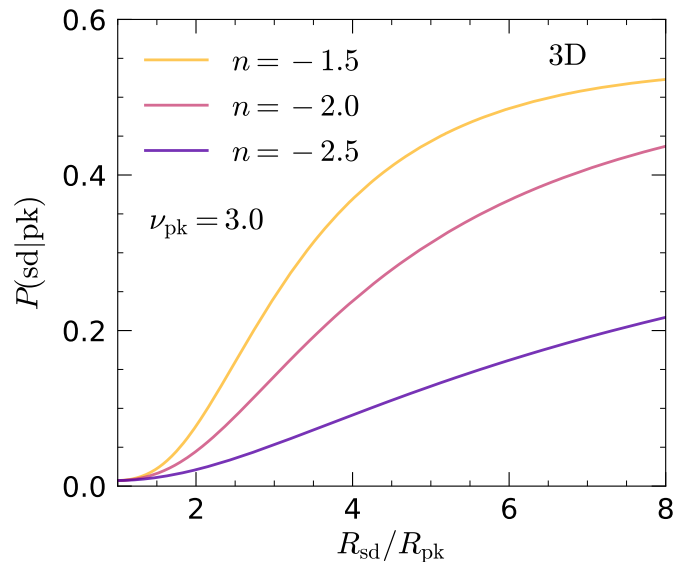


Fig. C.4. Similar to Figure 1, but for peaks with rarity $\nu_{\text{pk}} \geq 3$ in a 3D GRF with power-law spectra, computed using Equation (1). Only numerical results are shown, because analytical expressions are not available in 3D.

for $n = -2.5$, where we find a growing deviation from the fit with decreasing ν_{pk} . These power-law results provide a theoretical benchmark for interpreting the Λ CDM results discussed in the main text (in Figures 1 and 2), and in the next Appendix.

Appendix D: Λ CDM versus Power-Law spectra

The key distinguishing feature of the realistic Λ CDM model is the scale dependence of the effective spectral slope. To facilitate comparison with power-law results, we can define an effective spectral index, n_{eff} , which characterizes the slope of the Λ CDM

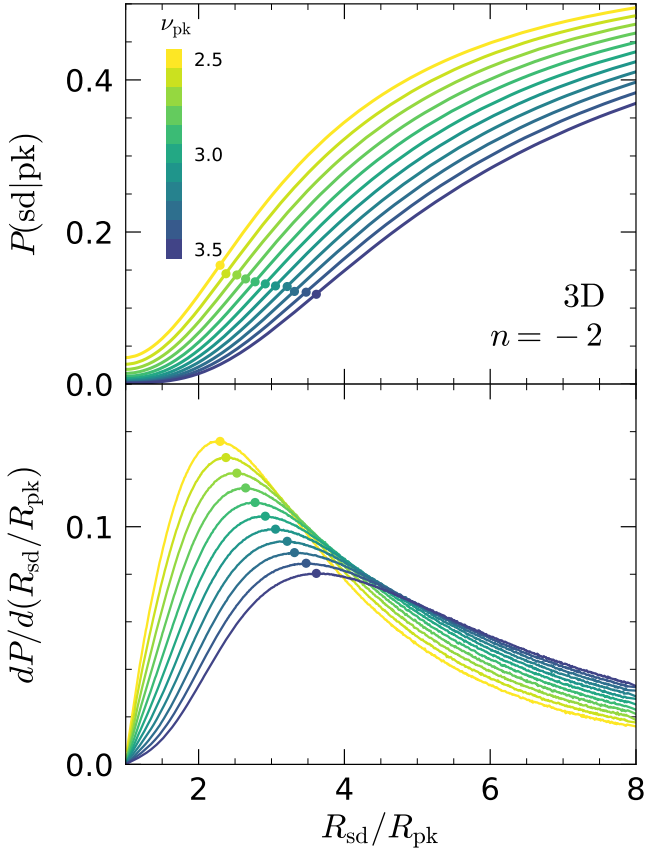


Fig. C.5. Similar to Figure C.2, but for a three dimensional GRF with a power law power spectrum, $P(k) \propto k^{-2}$. Only numerical results are shown, for 10 equally-spaced ν_{pk} . Qualitatively, the realm of filaments for 3D power-law power spectra are consistent with those in 2D.

power spectrum when smoothed on different scale R ,

$$n_{\text{eff}} \equiv -3 - \frac{d \log \sigma^2(R)}{d \log R}. \quad (\text{D.1})$$

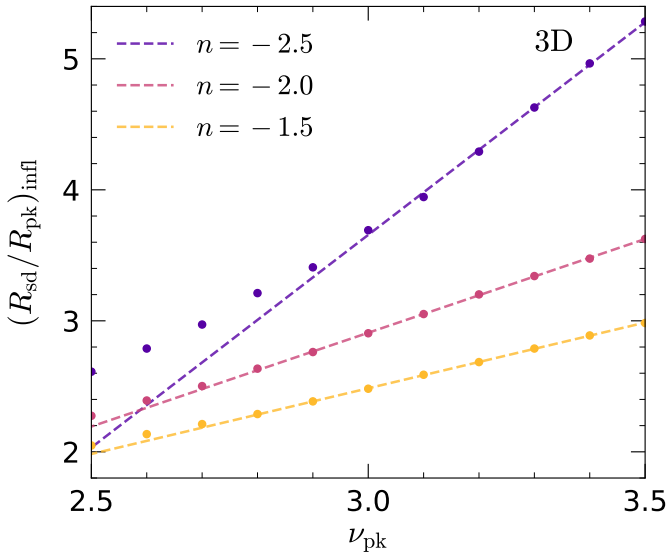


Fig. C.6. Similar to Figure 2, but for power-law power spectra. The dots are numerical results, and dashed lines are linear fits derived from data points with $\nu_{\text{pk}} \geq 3$. Qualitatively, these power-law results for the realm of filaments are consistent with the Λ CDM power spectrum.

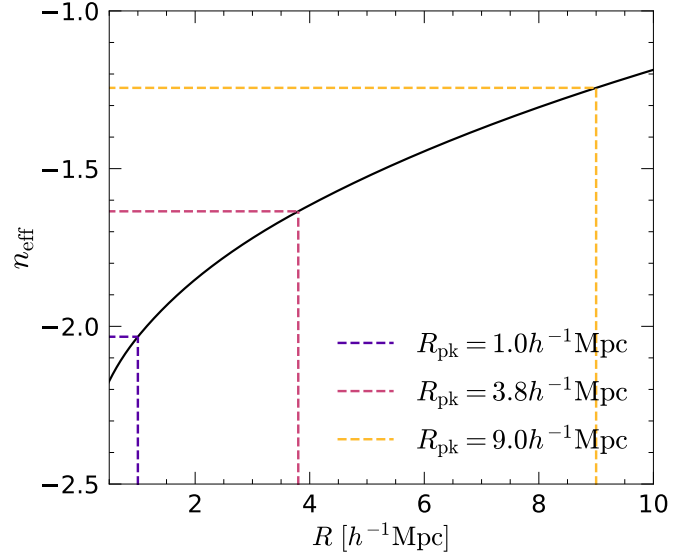


Fig. D.1. Effective spectral index for a Λ CDM power spectrum as a function of the Gaussian smoothing scale. Dashed lines mark the effective spectral indices corresponding to the peak sizes we considered in this analysis. The middle value is equivalent to a $8 h^{-1} \text{Mpc}$ top-hat smoothing. The effective spectral index increases toward a larger smoothing scale.

Here, $\sigma^2(R)$ denotes the variance of matter density fluctuations smoothed with a Gaussian filter. For a power-law spectrum $P_m(k) \propto k^n$, this definition simply gives $n_{\text{eff}} = n$.

The relation between the Gaussian smoothing scale (in the units of $h^{-1} \text{Mpc}$) and the effective spectral index is shown in Figure D.1, and can be approximated¹² as

$$n_{\text{eff}} \approx -2.35 + 0.36 \sqrt{R} + 0.064 \log R, \quad (\text{D.2})$$

which provides a mapping between Λ CDM and power-law power spectra models. Since the Λ CDM power spectrum smoothed on a smaller scale yields more negative n_{eff} , the observed trends – higher conditional probabilities and smaller characteristic scale ratios for a larger peak – are consistent with the behaviors shown in the power-law spectra analysis. We note that the enclosed masses of halos with top-hat radii corresponding to Gaussian $R_{\text{pk}} = 1.0, 3.8,$ and $9 h^{-1} \text{Mpc}$ are $M = 3.4 \times 10^{12}, 1.8 \times 10^{14}$ and $2.4 \times 10^{15} h^{-1} M_{\odot}$ at $z = 0$, respectively.

Power law spectra also provide an analytic form for the redshift dependence of the filamentary scale around the objects collapsing at a given z . Given that on the one hand, $\sigma_0(R_{\text{pk}}) = \sigma_8(R_8/R_{\text{pk}})^{(n+d)/2}$, where R_8 is a normalization scale, and, that on the other hand, $\sigma_0(R_{\text{pk}}) = \delta_c/D(z)\nu_{\text{pk}}$ from the criterion of collapse, we obtain from Equation B.4

$$R_{\text{sd}} = R_8 \left(\frac{D(z)\sigma_8\nu_{\text{pk}}}{\delta_c\gamma_*} \right)^{\frac{2}{n+d}} \left(1 + \sqrt{1 - \gamma_*^{\frac{4}{n+d}}} \right). \quad (\text{D.3})$$

Thus, for the power-law spectra $R_{\text{sd}} \propto D(z)^{2/(n+d)}$, i.e., $R_{\text{sd}} \propto (1+z)^{-2/(3+n)}$ in an Einstein-De Sitter universe.

In a Λ CDM universe, the spectrum is not scale-invariant, as illustrated in Figure D.2, and the growing mode likewise departs from $(1+z)^{-1}$. Therefore, here we provide a fitting form for

¹² it is accurate over the range $0.05 < R/h^{-1}(\text{Mpc}) < 20$ of Gaussian scales.

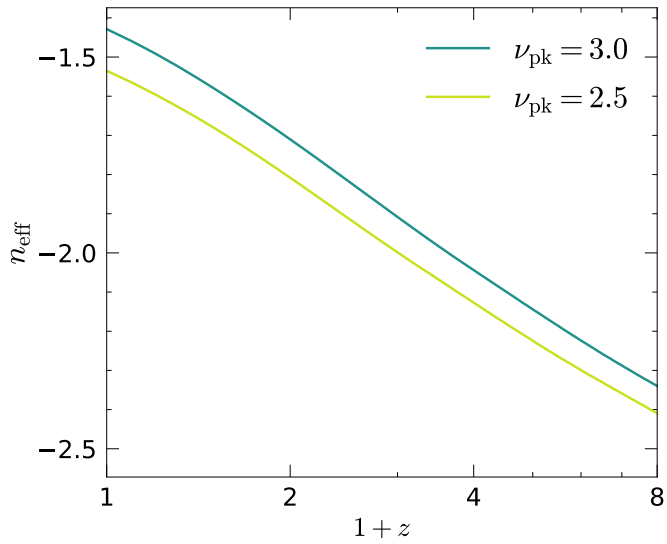


Fig. D.2. Effective spectral index for a Λ CDM power spectrum at the scale of the peaks with $\nu_{\text{pk}} = 3.0$ and 2.5 , collapsed at redshift z . The effective spectral index decreases toward higher redshifts.

the characteristic scale of filaments as a function of redshift in Λ CDM cosmology, which remains accurate to within 3%:

$$R_{\text{sd}}[h^{-1}\text{Mpc}] = \begin{cases} \frac{43 - 3.3(1+z)}{2.8 + (1+z)^2} & \text{for } \nu_{\text{pk}} = 2.5, \\ \frac{76.4 - 4.6(1+z)}{3.7 + (1+z)^2} & \text{for } \nu_{\text{pk}} = 3.0, \end{cases} \quad (\text{D.4})$$

In closing, the power-law results presented in Appendices [B](#), [C](#) and [D](#) robustly validate our main finding presented in Equations [\(7\)](#), [\(12\)](#), [\(13\)](#) and [\(14\)](#).